Solar Physics (2023) 298:87
https://doi.org/10.1007/s11207-023-02180-z

RESEARCH

Generating Photospheric Vector Magnetograms of Solar Active Regions for SOHO/MDI Using SDO/HMI and BBSO Data with Deep Learning

Haodi Jiang[1,2] · Qin Li[1,3] · Nian Liu[1,3] · Zhihang Hu[1] · Yasser Abduallah[1,4] · Ju Jing[1,3,5] · Yan Xu[1,3,5] · Jason T.L. Wang[1,4] · Haimin Wang[1,3,5]

Received: 27 November 2022 / Accepted: 12 June 2023 / Published online: 13 July 2023
© The Author(s), under exclusive licence to Springer Nature B.V. 2023

Abstract
Solar activity is often caused by the evolution of solar magnetic fields. Magnetic field parameters derived from photospheric vector magnetograms of solar active regions (ARs) have been used to analyze and forecast eruptive events, such as solar flares and coronal mass ejections. Unfortunately, the most recent Solar Cycle 24 was relatively weak with few large flares, though it is the only solar cycle in which consistent time-sequence vector magnetograms have been available through the *Helioseismic and Magnetic Imager* (HMI) on board the *Solar Dynamics Observatory* (SDO) since its launch in 2010. In this work, we look into another major instrument, namely the *Michelson Doppler Imager* (MDI) on board the *Solar and Heliospheric Observatory* (SOHO) from 1996 to 2010. The data archive of SOHO/MDI covers a more active Solar Cycle 23 with many large flares. However, SOHO/MDI only has line-of-sight (LOS) magnetograms. We propose a new deep learning method, named MagNet, to learn from combined LOS magnetograms, B_x and B_y, taken by SDO/HMI, along with Hα observations collected by the *Big Bear Solar Observatory* (BBSO), and to generate synthetic vector components B'_x and B'_y of ARs. These generated vector components, together with observational LOS data, would form vector magnetograms for SOHO/MDI. In this way, we can expand the availability of vector magnetograms to the period from 1996 to present. Experimental results demonstrate the good performance of the MagNet method. To our knowledge, this is the first time that deep learning has been used to generate photospheric vector magnetograms of ARs for SOHO/MDI using SDO/HMI and Hα data.

Keywords Magnetic fields · Photosphere · Neural networks · Data analysis

1. Introduction

Photospheric vector magnetograms of solar active regions (ARs) collected by the *Helioseismic and Magnetic Imager* (HMI) on board the *Solar Dynamics Observatory* (SDO; Scherrer et al., 2012) play an important role in solar physics. They are used by nonlinear force-free field extrapolation methods (Wheatland, Sturrock, and Roumeliotis, 2000; Wiegelmann, 2004; Metcalf, Leka, and Mickey, 2005; Schrijver et al., 2008; Sun et al., 2012) to calculate magnetic energy, which provides crucial information concerning the capability of an AR

Extended author information available on the last page of the article

for producing eruptive events including solar flares and coronal mass ejections (CMEs; Aschwanden, Xu, and Jing, 2014). They are also used to derive magnetic-field parameters, such as those of Space-weather HMI Active Region Patches (SHARP; Bobra et al., 2014), which have been used in machine learning-based flare and CME forecasting (Bobra and Couvidat, 2015; Chen et al., 2019; Liu et al., 2019, 2020b; Wang et al., 2020; Abduallah et al., 2021).

Since 2010, consistent time-sequence full-disk photospheric vector magnetograms have been available through SDO/HMI. This data set covers a relatively weak solar cycle, namely Cycle 24, which had fewer large eruptive events, and therefore the sampling is not sufficient to understand the initiation of solar eruptions and to make accurate prediction of eruptive events. Prior to 2010, vector magnetograms were available sporadically for certain ARs from some observatories, such as *Big Bear Solar Observatory* (BBSO; Denker et al., 1999), the *Synoptic Optical Long-term Investigations of the Sun* (SOLIS; Keller, Harvey, and Giampapa, 2003) of the *National Solar Observatory* (NSO), the *Imaging Vector Magnetograph* (IVM; Mickey et al., 1996) and *Haleakala Stokes Polarimeter* (HSP; Mickey, 1985) at the *Mees Solar Observatory* (MSO), the *National Astronomical Observatory of Japan* (NAOJ; Ichimoto et al., 1991), and the *Solar Optical Telescope Spectro-Polarimeter* (SOT-SP; Tsuneta et al., 2008) on board the *Hinode* spacecraft (Kosugi et al., 2007). However, these vector magnetograms were not consistently available. On the other hand, prior to 2010, full-disk line-of-sight (LOS) magnetograms have been consistently available from another source: the *Michelson Doppler Imager* (MDI) on board the *Solar and Heliospheric Observatory* (SOHO; Scherrer et al., 1995). This motivates us to develop a deep learning method, named MagNet, to generate consistent time-sequence vector magnetograms of all ARs from 1996 to 2010, which cover a more active Solar Cycle 23. Our MagNet model is trained by LOS magnetograms, B_x, B_y from SDO/HMI, combined with Hα observations from BBSO. The validation of our approach uses the overlapping data from 1 May 2010 to 11 April 2011 when MDI and HMI obtained data simultaneously. There is a good physical reason to use Hα as the additional constraint for this research: in the solar atmosphere, magnetic fields and flows are at a frozen-in condition, and therefore the Hα fibril structure can provide the direction of magnetic fields on the horizontal solar surface direction, X and Y dimensions (Wiegelmann et al., 2008; Jiang et al., 2021).

Deep learning has been widely used in solar physics (Benson et al., 2020; dos Santos et al., 2020; Jiang et al., 2020; Liu et al., 2021; Jiang et al., 2022). Recently, deep learning was employed to construct magnetograms and estimate magnetic fields. Kim et al. (2019) generated farside solar magnetograms from the *Solar-Terrestrial Relations Observatory* (STEREO)/*Extreme UltraViolet Imager* (EUVI) 304 Å images using a conditional generative adversarial network (cGAN). The authors trained their cGAN model using pairs of SDO/*Atmospheric Imaging Assembly* (AIA) 304 Å images and SDO/HMI magnetograms. Bai et al. (2021) estimated the unsigned radial component of the magnetic field from photospheric continuum images using a convolutional neural network (CNN). Dhuri et al. (2022) estimated vector field features of SHARP data using the LOS magnetograms from space-based SDO/HMI (specifically, the hmi.sharp_cea_720s data series) and ground-based GONG (*Global Oscillations Network Group*).

Our work differs from the above approaches in three ways. (1) Our trained MagNet model takes as input LOS magnetograms from SOHO/MDI together with Hα images from BBSO and generates as output magnetic field components B_x and B_y images, instead of estimating the SHARP features as done in Dhuri et al. (2022). (2) Our work utilizes BBSO Hα observations, which none of the above approaches use, to provide the direction information of magnetic fields in X and Y dimensions. (3) We use the full-disk magnetograms taken from the mdi.fd_M_96m_lev182, hmi.M_720s, hmi.B_720s data series, and design an algorithm to crop the AR patches from the full-disk magnetograms. The AR patches used in

our work are different from the ARs of SHARP. The generated/predicted B'_x and B'_y components along with the LOS components of the magnetic field, which can be treated as B_z components, of the AR patches create vector magnetograms from 1996 to 2010.

The rest of this article is organized as follows. Section 2 describes solar observations and our data preparation processes. Section 3 presents details of our MagNet model. Section 4 reports experimental results. Section 5 presents a discussion and concludes the article.

2. Observations and Data Preparation

MDI (Scherrer et al., 1995), which is part of the SOHO satellite, acquired a LOS magnetogram every 96 minutes during the period from 1995 to 2011, which covers the more active Solar Cycle 23 with many large flares. The spatial resolution is $4''$ and the full-disk images are collected on a 1024×1024 detector. As a successor of MDI, the HMI instrument, which is part of the SDO mission, provides continuous coverage of full-disk Doppler velocities, LOS magnetograms, and continuum proxy images (Scherrer et al., 2012). HMI has been operational since 1 May 2010, covering Solar Cycle 24. HMI observes the full solar disk at 6173 Å every 12 minutes for a better signal-to-noise ratio. The spatial resolution is $1''$ and the full-disk images are collected on a 4096×4096 detector. Photospheric vector magnetograms have been available since the launch of SDO/HMI. BBSO, which is a ground-based observatory, has provided Hα observations (images) since the 1970s (Denker et al., 1999). BBSO's full-disk Hα observations are taken every 1 minute, up to 9 hours for one observing day at the wavelength of 6563 Å. The spatial resolution is $2''$ and the full-disk images are collected on a 2048×2048 detector. Unlike satellite-based instruments such as MDI and HMI, the ground-based full-disk telescope at BBSO sometimes has seeing limitations due to unstable conditions of the Earth's atmosphere and weather.

In this study, we select full-disk Hα images based on three criteria. First, the selected images must be intact. Some images are incomplete due to (i) operating problems, such as incorrect angles of the telescope, loss of focus, sudden shaking of the telescope, etc., or (ii) external blocking entities such as birds, airplanes, etc. These incomplete images are excluded. Second, the selected images must show a clear appearance of the solar disk. Those images with unbalanced brightness caused by high and thin clouds are excluded. Third, among the images with a very close appearance, where the identifiable items on the solar disk do not have observable changes, the clearest one is selected. When items like active regions and filaments are close to the limb, which is darker than the solar center, we manually check if the items are clear. The images with a very close appearance and less clear items are excluded.

In this way, we select full-disk Hα images in the period from 1 May 2010 to 31 December 2017. For each selected full-disk Hα image, we collect its temporally closest full-disk MDI LOS magnetogram, full-disk HMI LOS magnetogram, and full-disk HMI vector magnetograms/components B_x, B_y, where the difference between the time stamp of the full-disk Hα image and the time stamp of a collected full-disk magnetogram has to be less than 6 minutes. We note that the full-disk MDI LOS magnetograms are only available from 1 May 2010 to 11 April 2011 within the period between 1 May 2010 and 31 December 2017. The full-disk Hα image and the full-disk MDI LOS magnetogram are linearly interpolated to the same spatial size of the full-disk HMI LOS magnetogram and HMI vector magnetograms/components B_x, B_y using the Interactive Data Language (IDL). These full-disk MDI LOS magnetograms (HMI LOS magnetograms, HMI vector magnetograms/components B_x, B_y, respectively) are taken directly from the

mdi.fd_M_96m_lev182 (hmi.M_720s, hmi.B_720s respectively) series at the Joint Science Operations Center (JSOC), accessible at http://jsoc.stanford.edu/.

Because we are mainly interested in solar flares in ARs, we coalign and crop AR patches of 256 × 256 pixels that might produce flares from the full-disk images using a two-step coaligning and cropping procedure written in IDL as follows. First, we perform a full-disk coalignment among the full-disk images. Then, we coalign and crop the AR patches from the coaligned full-disk images by maximizing the Pearson correlation coefficient (CC, Galton, 1886; Pearson, 1895; Sen and Srivastava, 1990) among the AR patches. The coaligned AR patches with CC below a threshold are discarded. In the study presented here, the threshold is set to 0.85. The AR patch size of 256 × 256 is chosen for efficient model training purposes where the magnetic field strength at the center of each AR patch is greater than or equal to 1500 Gauss. A large AR is segmented into several patches, all of which are included and used for training. Notice that in cropping the AR patches (square regions) from the full-disk images/magnetograms, all the cropped AR patches are re-sized to 256 × 256. Some of the AR patches for training the MagNet model may be from the same active region on different days.

In preparing the training data, we select 3745 full-disk Hα images from 1 January 2014 to 31 December 2017 and their temporally closest full-disk HMI LOS magnetograms and full-disk HMI vector magnetograms/components B_x, B_y. Each time we coalign and crop AR patches from four full-disk images, namely a full-disk HMI LOS magnetogram, a full-disk HMI vector magnetogram/component B_x, a full-disk HMI vector magnetogram/component B_y, and their temporally closest full-disk Hα image, using the two-step procedure written by IDL as described above. As a result of this coaligning and cropping process, we obtain 9290 coalignments each containing four AR patches. Both the full-disk HMI vector magnetograms B_x, B_y and the AR patches of B_x, B_y, cropped from the full-disk magnetograms, are in the image coordinate system. The 9290 coalignments of AR patches are then stored in the training set, denoted Train_HMI, which is used to train our MagNet model where all pixels in the AR patches are used to train the model. The 9290 AR patches of B_x, B_y in Train_HMI are used as labels when optimizing the model.

The validation data contain 155 full-disk MDI LOS magnetograms, full-disk HMI LOS magnetograms, full-disk HMI vector magnetograms/components B_x and B_y from 1 May 2010 to 11 April 2011, and their temporally closest full-disk Hα images. During this period, when both MDI data and HMI data are available, we are able to obtain all the five types of full-disk images. We note that the 155 collections of full-disk images (validation data) are independent and disjoint from those full-disk images in the training set due to their different collecting periods.

In processing the validation data, each time we coalign and crop AR patches of 256 × 256 pixels that might produce flares from five full-disk images, namely a full-disk MDI LOS magnetogram, a full-disk HMI LOS magnetogram, a full-disk HMI vector component B_x, a full-disk HMI vector component B_y, and their temporally closest full-disk Hα image, using the two-step procedure written in IDL, as described above. We obtain 12 coalignments each containing five AR patches. We store the 12 coalignments of HMI LOS magnetograms, HMI vector component B_x, B_y, and Hα images in the Validate_HMI set, which is used to validate MagNet-generated B'_x, B'_y components of HMI. We store the 12 coalignments of MDI LOS magnetograms, HMI vector components B_x, B_y, and Hα images in the Validate_MDI set, which is used to validate MagNet-generated B'_x, B'_y components of MDI. Please note that our training set (Train_HMI) and validation sets (Validate_HMI and Validate_MDI) cover different periods, as pointed out above. Thus, the trained MagNet model can make predictions on data that it has never seen during training.

3. Methodology

3.1. The Workflow of MagNet

Figure 1 illustrates the workflow of MagNet. Collected full-disk images including BBSO Hα images, HMI LOS magnetograms, and HMI vector components B_x and B_y are shown in the gray dashed box, where an AR patch in a full-disk image is highlighted by a small yellow box. We process these full-disk images by coaligning and cropping the AR patch out of each full-disk image to produce coaligned AR patches of 256 $\times$ 256 pixels enclosed in the blue dashed box (step 1). During training, pairs of coaligned AR patches of BBSO Hα images and HMI LOS magnetograms are fed to the MagNet model, where the corresponding AR

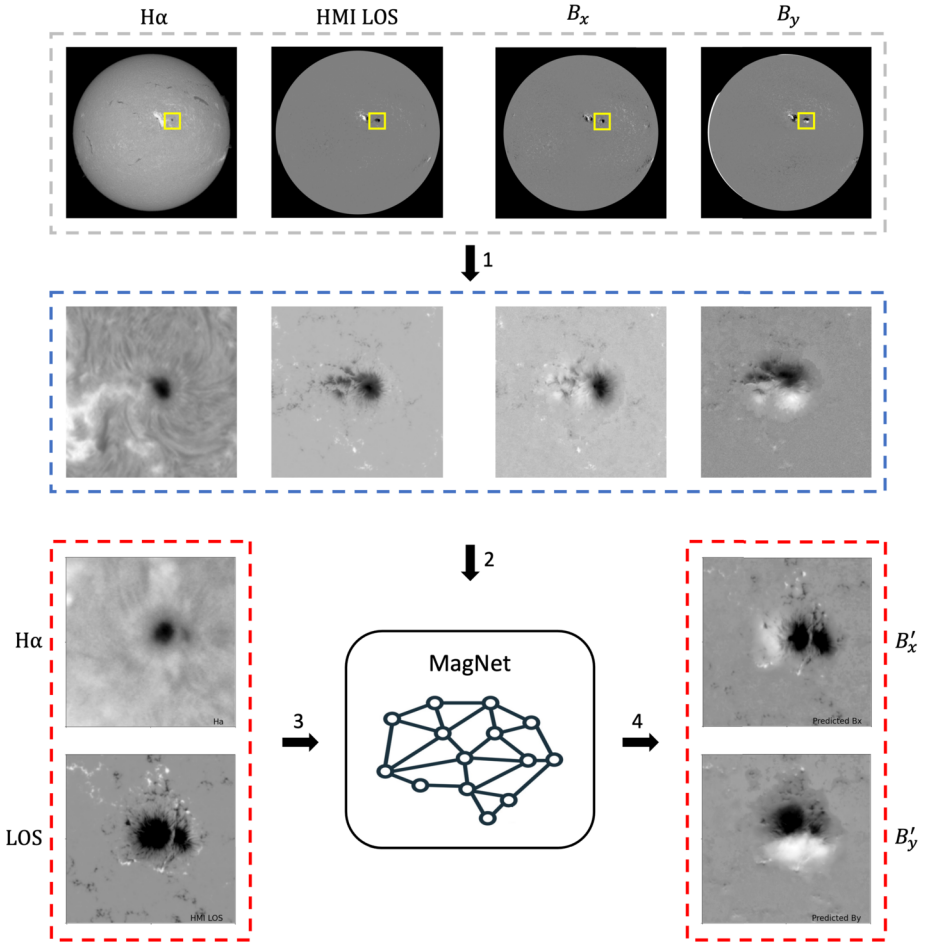

Figure 1 The workflow of MagNet. During training, we coalign and crop AR patches of 256 $\times$ 256 pixels from four full-disk images (step 1) and use the coaligned AR patches to train the MagNet model (step 2). During prediction, a pair of coaligned AR patches of Hα image and HMI/MDI LOS magnetogram is inputted to the trained Magnet model (step 3), which generates a pair of AR patches of B'_x and B'_y that correspond to the input data (step 4).

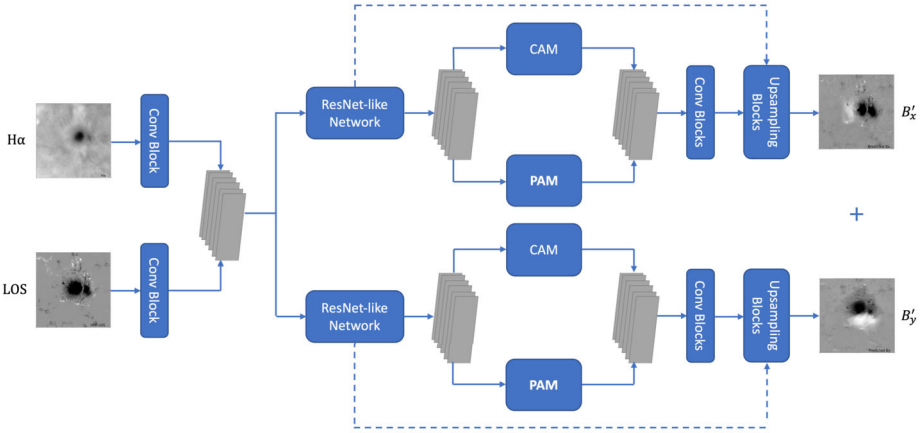

Figure 2 Illustration of the architecture of the MagNet model. The model takes as input a pair of coaligned AR patches of Hα image and HMI/MDI LOS magnetogram, and generates/predicts as output a pair of AR patches of B'_x and B'_y that correspond to the input data. See text for details of the model architecture.

patches of HMI vector components B_x and B_y, treated as true B_x and B_y, are used as labels (step 2). During prediction, the validation data containing a pair of coaligned AR patches of BBSO Hα image and HMI/MDI LOS magnetogram, shown in the left red dashed box, is inputted to the trained MagNet model (step 3). The model predicts (generates) a pair of AR patches of B'_x and B'_y, shown in the right red dashed box, that correspond to the input data (step 4).

3.2. The MagNet Model

Generating AR patches of B'_x and B'_y amounts to solving a regression problem because the output of the generating procedure consists of real numbers, i.e., magnetic field strengths. We employ a deep learning model containing a new CNN with self-attention (Zhao, Jia, and Koltun, 2020) to solve this regression problem. Self-attention was originally developed to learn global dependencies of input data and was used in machine translation (Vaswani et al., 2017). Later, self-attention was applied to many areas such as image recognition, scene segmentation, and image synthesis, etc. Figure 2 presents the architecture of our deep learning model.

During training, each pair of coaligned AR patches of BBSO Hα image and HMI LOS magnetogram taken from the training set, Train_HMI, is in turn fed to the MagNet model. The input images are first processed by convolutional blocks. Each convolutional block consists of a convolution layer with batch normalization, followed by a parametric ReLU (PReLU) activation function (He et al., 2015). The feature maps produced by the convolutional blocks are concatenated and sent to two separate paths, where one path generates an AR patch of B'_x and the other path generates an AR patch of B'_y that correspond to the input data. Each path starts with a ResNet-like network, specifically ResNet-101 (He et al., 2016) with dilated convolution (Zhang et al., 2018) as described in Fu et al. (2021). The output of the ResNet-like network is then sent to two modules: a channel attention module (CAM) and position attention module (PAM) (Fu et al., 2019). CAM and PAM leverage the self-attention mechanisms in the modules to better capture and transform a wider range of contextual information into local features, thus enhancing their representation capability.

CAM applies the self-attention mechanism to image channels, while PAM focuses on the calculation of location information. The outputs of CAM and PAM are combined and sent to convolutional blocks, followed by upsampling blocks that are convolutional blocks with upsampling and skip connection, represented as dashed lines in Figure 2 (Falk et al., 2019), to generate the AR patch of B'_x (B'_y, respectively). The AR patches of generated B'_x and B'_y are compared with labels (i.e., the corresponding AR patches of true B_x and B_y). The weights of neurons in the MagNet model are then updated to minimize the error (loss) caused by the comparison. At the end of the training process, the weights are optimized.

During validation, the trained MagNet model takes as input a pair of coaligned AR patches of a BBSO Hα image and HMI LOS magnetogram (MDI LOS magnetogram, respectively) taken from the Validate_HMI (Validate_MDI, respectively) set and generates as output a pair of AR patches of B'_x and B'_y that correspond to the input data. The AR patches of generated B'_x and B'_y are evaluated by the corresponding AR patches of HMI vector components B_x and B_y, treated as true B_x and B_y, in Validate_HMI (Validate_MDI, respectively).

For many of the AR patches used in our study, a large portion of each of them has small magnetic field strengths ($\leq$ 200 Gauss). Relatively few pixels in an AR patch have large magnetic field strengths ($>$ 200 Gauss). To tackle this imbalanced problem in our datasets, we employ a novel weighted L_w^p loss of a pixel p, defined as:

$$L_w^p(s', s) = |\frac{s}{c}||s' - s|. \tag{1}$$

Here, s' represents the MagNet-generated magnetic field strength at p, s represents the true magnetic field strength at p, and c is a threshold. In the study presented here, the threshold is set to 0.95. The absolute difference between s' and s at p, usually reflected by the L_1 loss, is multiplied by a weight, $|\frac{s}{c}|$. This suggests that a pixel p with a larger (smaller, respectively) magnetic field strength yields a larger (smaller, respectively) L_w^p loss.

The weighted loss between an AR patch, A, of generated B'_x and the corresponding AR patch of true B_x, denoted $L_w(B'_x, B_x)$, is defined as:

$$L_w(B'_x, B_x) = \frac{1}{N}\sum_{p\in A} L_w^p(s', s), \tag{2}$$

where $N = 256 \times 256 = 65{,}536$ is the total number of pixels in A. The weighted loss between an AR patch of generated B'_y and the corresponding AR patch of true B_y, denoted $L_w(B'_y, B_y)$, is defined similarly.

The total loss, denoted L_{MagNet}, is then defined as the sum of $L_w(B'_x, B_x)$ and $L_w(B'_y, B_y)$, as shown in Equation 3 below:

$$L_{MagNet} = L_w(B'_x, B_x) + L_w(B'_y, B_y). \tag{3}$$

The training of MagNet is done by applying the adaptive moment estimation (Adam) optimizer (Balles and Hennig, 2018) to minimize L_{MagNet} with 100 epochs on an NVIDIA A100 GPU.

4. Experiments and Results

4.1. Evaluation Metrics

We adopt three metrics, namely the mean absolute error (MAE; Sen and Srivastava, 1990), Pearson correlation coefficient (CC; Galton, 1886; Pearson, 1895; Sen and Srivastava, 1990), and percent agreement (PA; Liu et al., 2020a; Jiang et al., 2022) to quantitatively evaluate the performance of MagNet. The first metric is defined as:

$$\mathrm{MAE} = \frac{1}{N}\sum_{i=1}^{N}|s_i' - s_i|, \tag{4}$$

where $N = 65{,}536$ is the total number of pixels in an AR patch of a vector component, and s_i (s_i', respectively) denotes the true (generated, respectively) magnetic field strength for the ith pixel, $1 \le i \le 65{,}536$, in the vector component. This metric has a unit of Gauss, which is used to quantitatively assess the dissimilarity (distance) between the true magnetic field strengths and generated magnetic field strengths in the vector component.

The second metric is defined as:

$$\mathrm{CC} = \frac{\mathrm{E}[(T-\mu_T)(G-\mu_G)]}{\sigma_T\sigma_G}, \tag{5}$$

where $E(\cdot)$ is the expectation. T and G denote the true magnetic-field strengths and generated magnetic-field strengths, respectively, in the vector component. μ_T and μ_G denote the mean of T and G, respectively. σ_T and σ_G denote the standard deviation of T and G respectively. CC, which does not have units, has a value between -1 and 1. When CC is -1 or 1, there is an exact linear relationship between T and G. When CC is 0, there is no linear dependency between T and G.

The third metric is the percentage count of well-estimated pixels, which is defined as:

$$\mathrm{PA} = \frac{M}{N}\times 100\%, \tag{6}$$

where M denotes the total number of agreement pixels in the vector component. We say the ith pixel in the vector component is an agreement pixel if $|s_i - s_i'|$ is smaller than a user-specified threshold t. In the study presented here, the threshold t is set to 100 Gauss. This metric is used to quantitatively assess the similarity between the true magnetic field strengths and generated magnetic field strengths in the vector component.

4.2. Evaluation of MagNet

Table 1 presents the three evaluation metric values of MagNet based on the data in the Validate_HMI and Validate_MDI sets. Each triplet in the table consists of three values where the left one is the minimum value, the middle one is the average value, and the right one is the maximum value. The row of Validate_HMI(B_x') (Validate_HMI(B_y'), respectively) shows the metric values obtained by generating B_x' (B_y', respectively) based on the data in Validate_HMI. The row of Validate_MDI(B_x') (Validate_MDI(B_y'), respectively) shows the metric values obtained by generating B_x' (B_y', respectively) based on the data in Validate_MDI. The training data is from Train_HMI.

It can be seen from Table 1 that the generated B_x' (B_y', respectively) components are close to the true B_x (B_y, respectively) components with an average MAE being less than 100

Table 1 Evaluation metric values of MagNet based on validation data (see text).

Validation Data	MAE	CC	PA
Validate_HMI(B'_x)	(38.63, 58.16, 83.70)	(0.77, 0.87, 0.93)	(77.7%, 85.5%, 94.3%)
Validate_HMI(B'_y)	(43.26, 62.77, 91.10)	(0.79, 0.86, 0.93)	(79.6%, 82.7%, 91.8%)
Validate_MDI(B'_x)	(70.28, 90.71, 140.34)	(0.51, 0.73, 0.85)	(56.2%, 70.0%, 78.5%)
Validate_MDI(B'_y)	(57.52, 90.18, 131.26)	(0.62, 0.76, 0.85)	(54.4%, 69.3%, 85.8%)

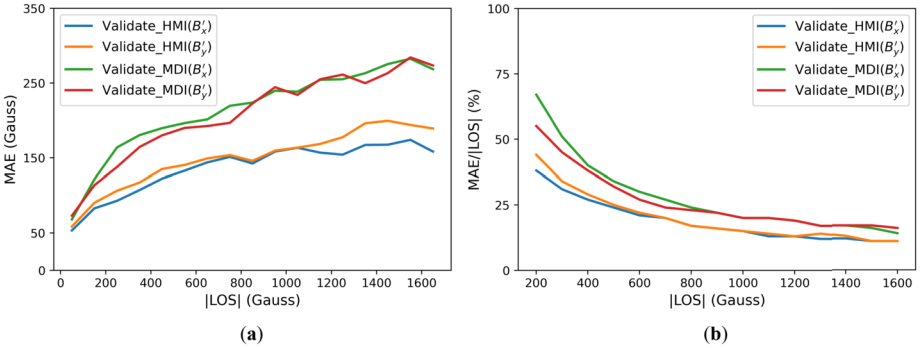

Figure 3 Plots showing how prediction errors of MagNet depend on |LOS| (absolute values of the field strengths of the LOS magnetograms in a validation set). (**a**) MAE as a function of |LOS|. (**b**) MAE/|LOS| as a function of |LOS|.

Gauss for both HMI and MDI. The average CC is approximately 0.87 for HMI and close to 0.75 for MDI. The average PA is approximately 84% for HMI and 70% for MDI. MagNet generally performs better for HMI than for MDI. This happens due to several reasons. First, the MagNet model is trained by HMI data, not MDI data. The spatial resolution of MDI images is 4″, which is lower than the resolution, 1″, of HMI images. Furthermore, due to the larger cadence (96 minutes) of MDI compared to the cadence (12 minutes) of HMI, the time gaps between the MDI images and their coaligned Hα images are often larger than the time gaps between the HMI images and their coaligned Hα images. As a result, the quality of the coalignments of AR patches for MDI is lower than the quality of the coalignments of AR patches for HMI.

Figure 3a shows the MAE values of the generated B'_x and B'_y components for HMI and MDI as a function of the absolute values of the magnetic field strengths of the LOS magnetograms (which are treated as B_z components), denoted by |LOS|, in the Validate_HMI and Validate_MDI sets. Here, each MAE value is calculated based on all pixels with the same field strength across all LOS magnetograms in a validation set. Figure 3b shows the proportion of MAE to |LOS| in percentage (i.e., relative error) as a function of |LOS|. It can be seen from Figure 3a that MAE (absolute error) increases as |LOS| increases. This happens because there are fewer pixels with larger field strengths. Although the absolute errors of the generated/predicted B'_x and B'_y components increase when observed |LOS| values increase, the relative errors decrease. It is noted from Figure 3b that the relative error (the ratio MAE/|LOS|) drops to 11% for HMI and 15% for MDI when |LOS| is 1500 Gauss.

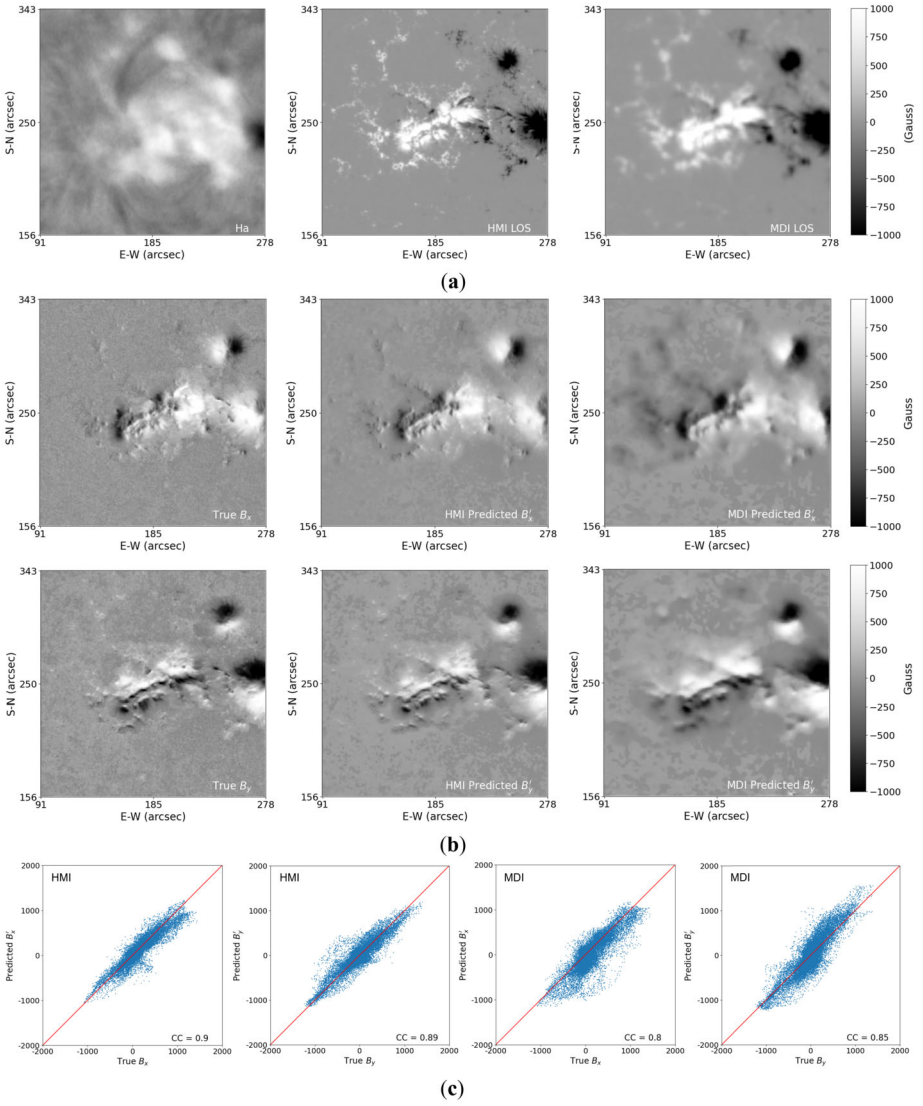

Figure 4 Comparison between the MagNet-generated B'_x, B'_y and true B_x, B_y of AR 11117 on 26 October 2010 at 22:24:00 UT. (**a**) BBSO Hα, HMI LOS, MDI LOS images inputted to MagNet. (**b**) True B_x, B_y, predicted B'_x, B'_y for HMI and predicted B'_x, B'_y for MDI. (**c**) Scatter plots of the predicted results versus true data.

4.3. A Case Study

To show how the degradation of the input magnetograms from HMI to MDI affects the predicted results, we present a case study on NOAA AR 11117 in the validation data. Figure 4 shows the generated B'_x and B'_y components for AR 11117 on 26 October 2010 at 22:24:00 UT where the training data is from Train_HMI. Figure 4a displays a coalignment of 256 × 256 patches of a BBSO Hα image, HMI LOS magnetogram, and MDI LOS magnetogram

from AR 11117. These images are inputted to the trained MagNet model. In Figure 4b, the first column shows the AR patches of true B_x and B_y components, the second column shows the AR patches of B'_x and B'_y components generated/predicted by MagNet using the BBSO Hα image and HMI LOS magnetogram in Figure 4a as input, and the third column shows the AR patches of B'_x and B'_y components generated/predicted by MagNet using the BBSO Hα image and MDI LOS magnetogram in Figure 4a as input. Figure 4c presents scatter plots. In each scatter plot, the X-axis represents the true B_x (B_y, respectively) and the Y-axis represents the generated/predicted B'_x (B'_y, respectively). The diagonal line in the scatter plot corresponds to pixels whose generated B'_x (B'_y, respectively) values are identical to the true B_x (B_y, respectively) values.

It can be seen from Figure 4b that MagNet works well on AR 11117, capable of generating the vector components that are close to the true components. The predicted B'_x and B'_y for HMI are visually more similar to the true B_x and B_y than those for MDI. More precisely, when using the BBSO Hα image and HMI LOS magnetogram as input, we obtain an MAE of 57.81 Gauss and 59.13 Gauss, a CC of 0.90 and 0.89, and a PA of 85.91% and 84.39% for B_x and B_y, respectively. On the other hand, when using the BBSO Hα image and MDI LOS magnetogram as input, we obtain an MAE of 85.41 Gauss and 87.98 Gauss, a CC of 0.80 and 0.85, and a PA of 72.77% and 69.30% for B_x and B_y, respectively. Thus, the evaluation metric values of the predicted B'_x and B'_y for MDI are worse than those of the predicted B'_x and B'_y for HMI.

4.4. Magnetic-Field Parameters Derived from NLFFFs

To demonstrate the usefulness of the magnetograms generated by MagNet, we attempt to derive magnetic field parameters, such as those in the SHARP dataset (Bobra et al., 2014), from the generated magnetograms. Notice that the AR patches used in our work are obtained from the cropping algorithm described in Section 2, which are different from the ARs in SHARP. Thus, it is difficult to directly compare the magnetic field parameters computed from MagNet-generated vector data with those in the SHARP dataset. Instead, we calculate and compare magnetic field parameters based on ground truth vector fields and MagNet-generated vector fields. Specifically, we calculate the parameters of total helicity and magnetic free energy using nonlinear force-free field (NLFFF) codes with the magnetograms as boundary conditions. The NLFFF extrapolation was performed with the weighted optimization method (Wiegelmann, 2004). A preprocessing scheme (Wiegelmann, Inhester, and Sakurai, 2006) is applied to make the boundary conditions agree to the force-free assumption. Again, we use AR 11117 as a case study and present results for this active region.

Figure 5 shows the distribution of the total helicity of different magnetograms, including the true magnetograms B from HMI (HMI true NLFFF), the predicted mangetograms B for HMI (HMI predicted NLFFF), and the predicted magnetograms B for MDI (MDI predicted NLFFF), on 26 October 2010 at 22:24:00 UT, 27 October 2010 at 22:24:00 UT, 28 October 2010 at 17:36:00 UT, respectively. It can be seen that there is a temporal and spatial consistency in the total helicity maps in Figure 5 with respect to the different input data (MDI or HMI) when compared to the HMI true data.

Figure 6 shows a temporal consistency of magnetic free energy of NLFFFs extrapolated with the true magnetograms from HMI (HMI true B), predicted magnetograms for HMI (HMI predicted B), and predicted magnetograms for MDI (MDI predicted B) as boundary conditions on 26 October 2010 at 22:24:00 UT, 27 October 2010 at 22:24:00 UT, 28 October 2010 at 17:36:00 UT, respectively. The free energy obtained from the predicted magnetograms is close to the free energy obtained from the true magnetograms, with the trends

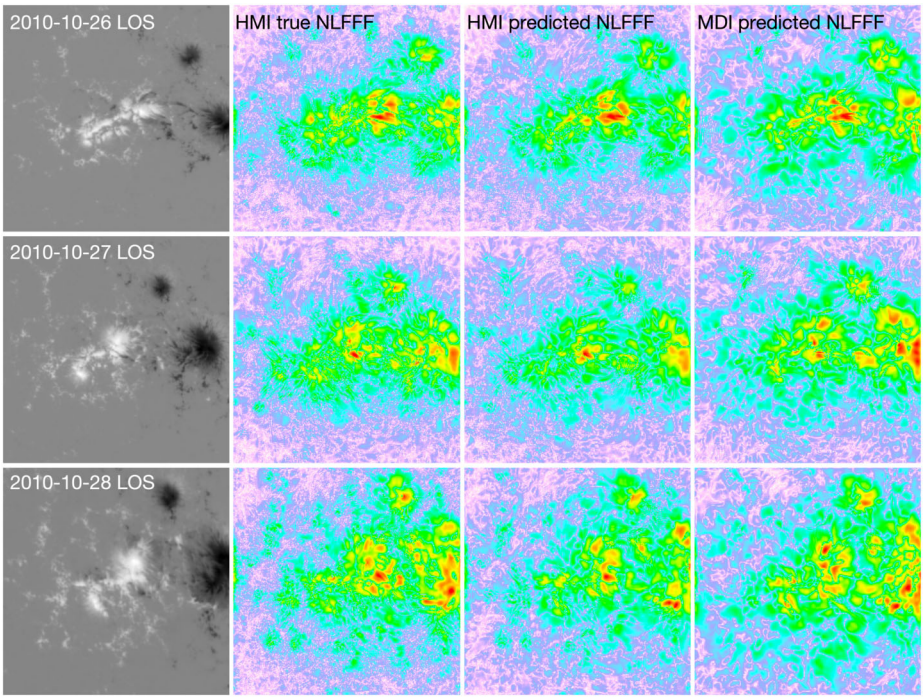

Figure 5 Total helicity maps on the photosphere calculated with NLFFF codes using the photospheric magneograms of HMI true B, HMI predicted B, and MDI predicted B as boundary conditions on 26 October 2010 at 22:24:00 UT, 27 October 2010 at 22:24:00 UT, 28 October 2010 at 17:36:00 UT, respectively. The panels in the left column show the corresponding HMI LOS magnetograms (treated as B_z here). B is comprised of B_x, B_y, and B_z components.

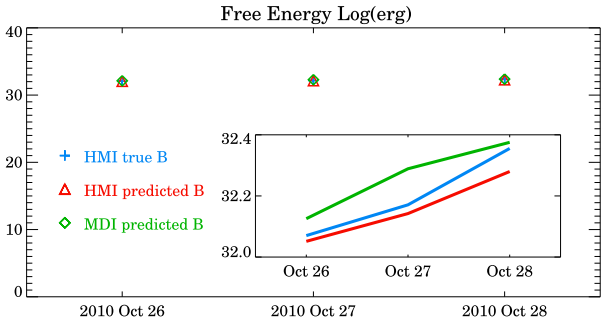

Figure 6 Magnetic free energy of NLFFFs extrapolated with the photospheric magnetograms of HMI true B, HMI predicted B, and MDI predicted B as boundary conditions on 26 October 2010 at 22:24:00 UT, 27 October 2010 at 22:24:00 UT, 28 October 2010 at 17:36:00 UT, respectively. The inset magnifies the variation by reducing the range on the Y-axis, demonstrating the extent of uncertainty and that the general trends agree between the true and predicted values.

and details shown in the inset of Figure 6. These results again demonstrate that MagNet-generated vector magnetograms are reasonably good compared to HMI true vector magnetograms.

5. Discussion and Conclusion

We present a deep learning method (MagNet) for generating photospheric vector magnetograms of solar active regions for SOHO/MDI using SDO/HMI and BBSO data. This method allows us to expand the availability of photospheric vector magnetograms to the period from 1996 to present, covering Solar Cycles 23 and 24. The vector magnetograms can be used by physics-based methods to calculate magnetic energy and magnetic field parameters useful for predicting solar flare activity (Liu et al., 2017, 2019, 2020b).

Our main results are listed below.

i) The experimental results obtained by using BBSO Hα observations and HMI magnetograms in the period between 1 January 2014 and 31 December 2017 as training data demonstrated the good performance of the proposed method. Refer to Table 1. When using the trained MagNet model to generate vector components B'_x and B'_y, based on BBSO Hα and HMI LOS data, and evaluated by HMI vector components B_x and B_y, we obtain on average MAE $\approx$ 60 Gauss, CC $\approx$ 0.87, and PA $\approx$ 84%. When using the trained MagNet model to generate vector components B'_x and B'_y, based on BBSO Hα and MDI LOS data, and evaluated by the same HMI vector components B_x and B_y, we obtain on average MAE $\approx$ 90 Gauss, CC $\approx$ 0.75, and PA $\approx$ 70%.

ii) When training and validating the MagNet model, we do not impose any threshold on the data. In other words, all pixels in the original images from the instruments (MDI, HMI, BBSO) are included. Notice that the HMI vector components B_x and B_y, treated as ground truth, in our study are originally obtained as a solution of the inverse problem using optimization methods (Hoeksema et al., 2014; Liu et al., 2020a; Jiang et al., 2022). The trained MagNet model inherits issues and limitations of the ground truth. This implies that disagreements with the ground truth are not necessarily dramatic.

iii) MagNet is trained by HMI data and validated on MDI data. However, HMI and MDI are two different instruments on different observatories with different temporal and spatial resolutions. One could use deep learning techniques (Menon et al., 2020; Danier, Zhang, and Bull, 2022; Rombach et al., 2022) to improve the temporal and spatial resolutions of the images from the different sources to enhance the performance of MagNet. Transfer learning could also be helpful in obtaining knowledge from one source and applying the knowledge to another source (Zhuang et al., 2021).

iv) Our approach depends on the coalignments of AR patches, which are produced by a two-step coaligning and cropping procedure, written by IDL, as described in Section 2. We discard coaligned AR patches whose coalignment accuracy (more precisely, Pearson correlation coefficient or CC) is below a threshold. When the threshold is 0.85, the performance of MagNet is quantified in Table 1. When the threshold is lower (e.g. 0.8), the performance of MagNet drops slightly. Consider, for example, AR 11117. When the threshold is 0.85, the CC obtained in generating HMI vector components B'_x and B'_y is 0.9 and 0.89, respectively. When the threshold is 0.8, the CC obtained in generating HMI vector components B'_x and B'_y is 0.88 and 0.87, respectively. Thus, MagNet is not very sensitive to the coalignment accuracy provided that the accuracy is sufficiently large. Coaligning images from different instruments is a challenge. Developing more accurate coalignment algorithms implemented in OpenCV or IDL may further improve the performance of MagNet.

v) BBSO's full-disk Hα observations have been collected every 1 minute since the 1970s. The observatory is operated approximately 6 hours on average, up to 9 hours when necessary, each day. Nevertheless, we may miss a portion of the Hα observations due to unstable conditions of the Earth's atmosphere and weather. It is estimated that 25%

of the MDI vector data in Solar Cycle 23, or fewer due to the removal of low-quality coalignments of MDI LOS magnetograms and Hα images, can be reconstructed with MagNet. To get full coverage of the ARs in Solar Cycle 23, one would need other sources of Hα data, particularly from the *Global Hα Network* (Steinegger et al., 2000). In fact, the *Kanzelhöhe Solar Observatory* (KSO; Otruba, 1999; Otruba, Freislich, and Hanslmeier, 2008) provides quite consistent Hα data. This would increase the availability of Hα images significantly and make the reconstruction of the majority of MDI vector magnetograms of solar ARs possible.

In conclusion, MagNet is the first method able to generate photospheric vector magnetograms of solar ARs for SOHO/MDI using SDO/HMI and Hα data. According to our experimental results, the vector components generated by MagNet are reasonably close to ground truth.

Acknowledgments SOHO is a project of international cooperation between ESA and NASA. SDO is a NASA mission. The BBSO operation is supported by the New Jersey Institute of Technology and U.S. NSF grant AGS-1821294. The MagNet model is implemented in Python and TensorFlow. This work was supported by U.S. NSF grants AGS-1927578, AGS-1954737, AGS-2149748 and AGS-2228996. We thank the handling editor and anonymous referee for the thoughtful comments and constructive suggestions that have helped us improve the presentation and content of this article.

Author contributions H.W. conceived the study. H.J. wrote the manuscript. All the authors reviewed the manuscript.

Data Availability The trained MagNet model and datasets used in this study can be downloaded from https://nature.njit.edu/solardb/magnet.

Declarations

Competing interests The authors declare no competing interests.

References

Abduallah, Y., Wang, J.T.L., Nie, Y., Liu, C., Wang, H.: 2021, DeepSun: machine-learning-as-a-service for solar flare prediction. *Res. Astron. Astrophys.* **21**(7), 160. DOI.

Aschwanden, M.J., Xu, Y., Jing, J.: 2014, Global energetics of solar flares. I. Magnetic energies. *Astrophys. J.* **797**(1), 50. DOI.

Bai, X., Liu, H., Deng, Y., Jiang, J., Guo, J., Bi, Y., Feng, T., Jin, Z., Cao, W., Su, J., Ji, K.: 2021, A deep learning method to estimate magnetic fields in solar active regions from photospheric continuum images. *Astron. Astrophys.* **652**, A143. DOI.

Balles, L., Hennig, P.: 2018, Dissecting Adam: the sign, magnitude and variance of stochastic gradients. In: *Proc. 35th Int. Conf. Machine Learning* **80**, 413. http://proceedings.mlr.press/v80/balles18a.html.

Benson, B., Pan, W.D., Prasad, A., Gary, G.A., Hu, Q.: 2020, Forecasting solar cycle 25 using deep neural networks. *Solar Phys.* **295**(5), 65. DOI.

Bobra, M.G., Couvidat, S.: 2015, Solar flare prediction using SDO/HMI vector magnetic field data with a machine-learning algorithm. *Astrophys. J.* **798**(2), 135. DOI.

Bobra, M.G., Sun, X., Hoeksema, J.T., Turmon, M., Liu, Y., Hayashi, K., Barnes, G., Leka, K.D.: 2014, The Helioseismic and Magnetic Imager (HMI) vector magnetic field pipeline: SHARPs - space-weather HMI active region patches. *Solar Phys.* **289**(9), 3549. DOI.

Chen, Y., Manchester, W.B., Hero, A.O., Toth, G., DuFumier, B., Zhou, T., Wang, X., Zhu, H., Sun, Z., Gombosi, T.I.: 2019, Identifying solar flare precursors using time series of SDO/HMI images and SHARP parameters. *Space Weather* **17**(10), 1404. DOI.

Danier, D., Zhang, F., Bull, D.R.: 2022, ST-MFNet: a spatio-temporal multi-flow network for frame interpolation. In: *IEEE/CVF Conf. Computer Vision and Pattern Recognition*, 3511. DOI.

Denker, C., Johannesson, A., Marquette, W., Goode, P.R., Wang, H., Zirin, H.: 1999, Synoptic Hα full-disk observations of the sun from big bear solar observatory - I. Instrumentation, image processing, data products, and first results. *Solar Phys.* **184**(1), 87. DOI.

Dhuri, D.B., Bhattacharjee, S., Hanasoge, S.M., Kiran Mahapatra, S.: 2022, Deep-learning reconstruction of sunspot vector magnetic fields for forecasting solar storms. *Astrophys. J.* **939**(2), 64. DOI.

dos Santos, L.F.G., Narock, A., Nieves-Chinchilla, T., Nuñez, M., Kirk, M.: 2020, Identifying flux rope signatures using a deep neural network. *Solar Phys.* **295**(10), 131. DOI.

Falk, T., Mai, D., Bensch, R., Çiçek, Ö., Abdulkadir, A., Marrakchi, Y., Böhm, A., Deubner, J., Jäckel, Z., Seiwald, K., Dovzhenko, A., Tietz, O., Dal Bosco, C., Walsh, S., Saltukoglu, D., Tay, T.L., Prinz, M., Palme, K., Simons, M., Diester, I., Brox, T., Ronneberger, O.: 2019, U-Net: deep learning for cell counting, detection, and morphometry. *Nat. Methods* **16**(1), 67. DOI.

Fu, J., Liu, J., Tian, H., Li, Y., Bao, Y., Fang, Z., Lu, H.: 2019, Dual attention network for scene segmentation. In: *IEEE Conf. Computer Vision and Pattern Recognition*, 3146. DOI.

Fu, J., Liu, J., Jiang, J., Li, Y., Bao, Y., Lu, H.: 2021, Scene segmentation with dual relation-aware attention network. *IEEE Trans. Neural Netw. Learn. Syst.* **32**(6), 2547. DOI.

Galton, F.: 1886, Regression towards mediocrity in hereditary stature. *J. Anthropol. Inst. G. B. Irel.* **15**, 246. DOI.

He, K., Zhang, X., Ren, S., Sun, J.: 2015, Delving deep into rectifiers: surpassing human-level performance on ImageNet classification. In: *IEEE Int. Conf. Computer Vision*, 1026. DOI.

He, K., Zhang, X., Ren, S., Sun, J.: 2016, Deep residual learning for image recognition. In: *IEEE Conf. Computer Vision and Pattern Recognition*, 770. DOI.

Hoeksema, J.T., Liu, Y., Hayashi, K., Sun, X., Schou, J., Couvidat, S., Norton, A., Bobra, M., Centeno, R., Leka, K.D., Barnes, G., Turmon, M.: 2014, The helioseismic and magnetic imager (HMI) vector magnetic field pipeline: overview and performance. *Solar Phys.* **289**(9), 3483. DOI.

Ichimoto, K., Sakurai, T., Yamaguchi, A., Kumagai, K., Nishino, Y., Suematsu, Y., Hiei, E., Hirayama, T.: 1991, Solar flare telescope and 10-cm new coronagraph. In: Uchida, Y., Canfield, R.C., Watanabe, T., Hiei, E. (eds.) *Flare Physics in Solar Activity Maximum* **22**, 320. DOI.

Jiang, H., Wang, J., Liu, C., Jing, J., Liu, H., Wang, J.T.L., Wang, H.: 2020, Identifying and tracking solar magnetic flux elements with deep learning. *Astrophys. J. Suppl.* **250**(1), 5. DOI.

Jiang, H., Jing, J., Wang, J., Liu, C., Li, Q., Xu, Y., Wang, J.T.L., Wang, H.: 2021, Tracing Hα fibrils through Bayesian deep learning. *Astrophys. J. Suppl.* **256**(1), 20. DOI.

Jiang, H., Li, Q., Xu, Y., Hsu, W., Ahn, K., Cao, W., Wang, J.T.L., Wang, H.: 2022, Inferring line-of-sight velocities and Doppler widths from Stokes profiles of GST/NIRIS using stacked deep neural networks. *Astrophys. J.* **939**(2), 66. DOI.

Keller, C.U., Harvey, J.W., Giampapa, M.S.: 2003, SOLIS: an innovative suite of synoptic instruments. In: Keil, S.L., Avakyan, S.V. (eds.) *Innovative Telescopes and Instrumentation for Solar Astrophysics*, *SPIE Conf. Ser.* **4853**, 194. DOI.

Kim, T., Park, E., Lee, H., Moon, Y.-J., Bae, S.-H., Lim, D., Jang, S., Kim, L., Cho, I.-H., Choi, M., Cho, K.-S.: 2019, Solar farside magnetograms from deep learning analysis of STEREO/EUVI data. *Nat. Astron.* **3**, 397. DOI.

Kosugi, T., Matsuzaki, K., Sakao, T., Shimizu, T., Sone, Y., Tachikawa, S., Hashimoto, T., Minesugi, K., Ohnishi, A., Yamada, T., Tsuneta, S., Hara, H., Ichimoto, K., Suematsu, Y., Shimojo, M., Watanabe, T., Shimada, S., Davis, J.M., Hill, L.D., Owens, J.K., Title, A.M., Culhane, J.L., Harra, L.K., Doschek, G.A., Golub, L.: 2007, The Hinode (Solar-B) mission: an overview. *Solar Phys.* **243**(1), 3. DOI.

Liu, C., Deng, N., Wang, J.T.L., Wang, H.: 2017, Predicting solar flares using SDO/HMI vector magnetic data products and the random forest algorithm. *Astrophys. J.* **843**(2), 104. DOI.

Liu, H., Liu, C., Wang, J.T.L., Wang, H.: 2019, Predicting solar flares using a long short-term memory network. *Astrophys. J.* **877**(2), 121. DOI.

Liu, H., Liu, C., Wang, J.T.L., Wang, H.: 2020b, Predicting coronal mass ejections using SDO/HMI vector magnetic data products and recurrent neural networks. *Astrophys. J.* **890**(1), 12. DOI.

Liu, H., Xu, Y., Wang, J., Jing, J., Liu, C., Wang, J.T.L., Wang, H.: 2020a, Inferring vector magnetic fields from Stokes profiles of GST/NIRIS using a convolutional neural network. *Astrophys. J.* **894**(1), 70. DOI.

Liu, J., Wang, Y., Huang, X., Korsós, M.B., Jiang, Y., Wang, Y., Erdélyi, R.: 2021, Reliability of AI-generated magnetograms from only EUV images. *Nat. Astron.* **5**, 108. DOI.

Menon, S., Damian, A., Hu, S., Ravi, N., Rudin, C.: 2020, PULSE: self-supervised photo upsampling via latent space exploration of generative models. In: *IEEE/CVF Conf. Computer Vision and Pattern Recognition*, 2434. DOI.

Metcalf, T.R., Leka, K.D., Mickey, D.L.: 2005, Magnetic free energy in NOAA active region 10486 on 2003 October 29. *Astrophys. J. Lett.* **623**(1), L53. DOI.

Mickey, D.L.: 1985, The Haleakala Stokes polarimeter. *Solar Phys.* **97**(2), 223. DOI.

Mickey, D.L., Canfield, R.C., Labonte, B.J., Leka, K.D., Waterson, M.F., Weber, H.M.: 1996, The imaging vector magnetograph at Haleakala. *Solar Phys.* **168**(2), 229. DOI.
Otruba, W.: 1999, High cadence digital full disk Hα patrol device at Kanzelhöhe. *Third Adv. Solar Phys. Euroconf. Magnetic Fields and Oscillations* **184**, 314. ADS.
Otruba, W., Freislich, H., Hanslmeier, A.: 2008, Kanzelhöhe photosphere telescope (KPT). *Cent. Eur. Astrophys. Bull.* **32**, 1. ADS.
Pearson, K.: 1895, Notes on regression and inheritance in the case of two parents. *Proc. Roy. Soc. London* **58**(347–352), 240. DOI.
Rombach, R., Blattmann, A., Lorenz, D., Esser, P., Ommer, B.: 2022, High-resolution image synthesis with latent diffusion models. In: *IEEE/CVF Conf. Computer Vision and Pattern Recognition*, 10674. DOI.
Scherrer, P.H., Bogart, R.S., Bush, R.I., Hoeksema, J.T., Kosovichev, A.G., Schou, J., Rosenberg, W., Springer, L., Tarbell, T.D., Title, A., Wolfson, C.J., Zayer, I. (MDI Engineering Team): 1995, The solar oscillations investigation - Michelson Doppler imager. *Solar Phys.* **162**(1–2), 129. DOI.
Scherrer, P.H., Schou, J., Bush, R.I., Kosovichev, A.G., Bogart, R.S., Hoeksema, J.T., Liu, Y., Duvall, T.L., Zhao, J., Title, A.M., Schrijver, C.J., Tarbell, T.D., Tomczyk, S.: 2012, The Helioseismic and Magnetic Imager (HMI) Investigation for the Solar Dynamics Observatory (SDO). *Solar Phys.* **275**(1–2), 207. DOI.
Schrijver, C.J., DeRosa, M.L., Metcalf, T., Barnes, G., Lites, B., Tarbell, T., McTiernan, J., Valori, G., Wiegelmann, T., Wheatland, M.S., Amari, T., Aulanier, G., Démoulin, P., Fuhrmann, M., Kusano, K., Régnier, S., Thalmann, J.K.: 2008, Nonlinear force-free field modeling of a solar active region around the time of a major flare and coronal mass ejection. *Astrophys. J.* **675**(2), 1637. DOI.
Sen, A., Srivastava, M.: 1990, *Regression Analysis*, Springer, New York. DOI.
Steinegger, M., Denker, C., Goode, P.R., Marquette, W.H., Varsik, J., Wang, H., Otruba, W., Freislich, H., Hanslmeier, A., Luo, G., Chen, D., Zhang, Q.: 2000, The new global high-resolution Hα network: First observations and first results 463 617. ADS.
Sun, X., Hoeksema, J.T., Liu, Y., Wiegelmann, T., Hayashi, K., Chen, Q., Thalmann, J.: 2012, Evolution of magnetic field and energy in a major eruptive active region based on SDO/HMI observation. *Astrophys. J.* **748**(2), 77. DOI.
Tsuneta, S., Ichimoto, K., Katsukawa, Y., Nagata, S., Otsubo, M., Shimizu, T., Suematsu, Y., Nakagiri, M., Noguchi, M., Tarbell, T., Title, A., Shine, R., Rosenberg, W., Hoffmann, C., Jurcevich, B., Kushner, G., Levay, M., Lites, B., Elmore, D., Matsushita, T., Kawaguchi, N., Saito, H., Mikami, I., Hill, L.D., Owens, J.K.: 2008, The solar optical telescope for the Hinode mission: an overview. *Solar Phys.* **249**(2), 167. DOI.
Vaswani, A., Shazeer, N., Parmar, N., Uszkoreit, J., Jones, L., Gomez, A.N., Kaiser, L.u., Polosukhin, I.: 2017, Attention is all you need. *Adv. Neural Information Processing Systems* 30. https://papers.nips.cc/paper/2017/hash/3f5ee243547dee91fbd053C1C4a845aa-Abstract.html.
Wang, X., Chen, Y., Toth, G., Manchester, W.B., Gombosi, T.I., Hero, A.O., Jiao, Z., Sun, H., Jin, M., Liu, Y.: 2020, Predicting solar flares with machine learning: investigating solar cycle dependence. *Astrophys. J.* **895**(1), 3. DOI.
Wheatland, M.S., Sturrock, P.A., Roumeliotis, G.: 2000, An optimization approach to reconstructing force-free fields. *Astrophys. J.* **540**(2), 1150. DOI.
Wiegelmann, T.: 2004, Optimization code with weighting function for the reconstruction of coronal magnetic fields. *Solar Phys.* **219**(1), 87. DOI.
Wiegelmann, T., Inhester, B., Sakurai, T.: 2006, Preprocessing of vector magnetograph data for a nonlinear force-free magnetic field reconstruction. *Solar Phys.* **233**(2), 215. DOI.
Wiegelmann, T., Thalmann, J.K., Schrijver, C.J., De Rosa, M.L., Metcalf, T.R.: 2008, Can we improve the preprocessing of photospheric vector magnetograms by the inclusion of chromospheric observations? *Solar Phys.* **247**(2), 249. DOI.
Zhang, H., Dana, K.J., Shi, J., Zhang, Z., Wang, X., Tyagi, A., Agrawal, A.: 2018, Context encoding for semantic segmentation. In: *IEEE Conf. Computer Vision and Pattern Recognition*, 7151. DOI.
Zhao, H., Jia, J., Koltun, V.: 2020, Exploring self-attention for image recognition. In: *IEEE/CVF Conf. Computer Vision and Pattern Recognition*, 10073. DOI.
Zhuang, F., Qi, Z., Duan, K., Xi, D., Zhu, Y., Zhu, H., Xiong, H., He, Q.: 2021, A comprehensive survey on transfer learning. *Proc. IEEE* **109**(1), 43. DOI.

Publisher's Note Springer Nature remains neutral with regard to jurisdictional claims in published maps and institutional affiliations.

Springer Nature or its licensor (e.g. a society or other partner) holds exclusive rights to this article under a publishing agreement with the author(s) or other rightsholder(s); author self-archiving of the accepted manuscript version of this article is solely governed by the terms of such publishing agreement and applicable law.

Authors and Affiliations

Haodi Jiang[1,2] · Qin Li[1,3] · Nian Liu[1,3] · Zhihang Hu[1] · Yasser Abduallah[1,4] · Ju Jing[1,3,5] · Yan Xu[1,3,5] · Jason T.L. Wang[1,4] · Haimin Wang[1,3,5]

✉ H. Jiang
haodi.jiang@shsu.edu

J.T.L. Wang
wangj@njit.edu

H. Wang
haimin.wang@njit.edu

1 Institute for Space Weather Sciences, New Jersey Institute of Technology, University Heights, Newark, NJ 07102, USA

2 Department of Computer Science, Sam Houston State University, 1905 University Ave, Huntsville, TX 77341, USA

3 Center for Solar-Terrestrial Research, New Jersey Institute of Technology, University Heights, Newark, NJ 07102, USA

4 Department of Computer Science, New Jersey Institute of Technology, University Heights, Newark, NJ 07102, USA

5 Big Bear Solar Observatory, New Jersey Institute of Technology, 40386 North Shore Lane, Big Bear City, CA 92314, USA